Featured in Physics

Structural and electron spin state changes in an x-ray heated iron carbonate system at the Earth's lower mantle pressures

Johannes M. Kaa,[1,2,*] Christian Sternemann,[2] Karen Appel,[1] Valerio Cerantola,[1] Thomas R. Preston,[1] Christian Albers,[2] Mirko Elbers,[3] Lélia Libon,[3] Mikako Makita,[1] Alexander Pelka,[1] Sylvain Petitgirard,[4] Christian Plückthun,[1] Vladimir Roddatis,[5] Christoph J. Sahle,[6] Georg Spiekermann,[3,4] Christian Schmidt,[5] Anja Schreiber,[5] Robin Sakrowski,[2] Metin Tolan,[2,7] Max Wilke,[3] Ulf Zastrau,[1] and Zuzana Konôpková[1]

[1]*European XFEL, Holzkoppel 4, 22869 Schenefeld, Germany*

[2]*Technische Universität Dortmund, Fakultät Physik/DELTA, Maria-Goeppert-Mayer-Straße 2, 44227 Dortmund, Germany*

[3]*Universität Potsdam, Inst. f. Geowissenschaften, Karl-Liebknecht-Straße 24, 14476 Potsdam, Germany*

[4]*ETH Zürich, Rämistraß 101, 8092 Zürich, Switzerland*

[5]*Geoforschungszentrum Telegrafenberg, 14473 Potsdam, Germany*

[6]*ESRF, The European Synchrotron, 71 Avenue des Martyrs, CS40220, 38043 Grenoble Cedex 9, France*

[7]*Universität Göttingen, Wilhelmsplatz 1, 37073 Göttingen, Germany*

(Received 13 December 2021; accepted 26 May 2022; published 15 July 2022)

The determination of the spin state of iron-bearing compounds at high pressure and temperature is crucial for our understanding of chemical and physical properties of the deep Earth. Studies on the relationship between the coordination of iron and its electronic spin structure in iron-bearing oxides, silicates, carbonates, iron alloys, and other minerals found in the Earth's mantle and core are scarce because of the technical challenges to simultaneously probe the sample at high pressures and temperatures. We used the unique properties of a pulsed and highly brilliant x-ray free electron laser (XFEL) beam at the High Energy Density (HED) instrument of the European XFEL to x-ray heat and probe samples contained in a diamond anvil cell. We heated and probed with the same x-ray pulse train and simultaneously measured x-ray emission and x-ray diffraction of an $FeCO_3$ sample at a pressure of 51 GPa with up to melting temperatures. We collected spin state sensitive Fe $K\beta_{1,3}$ fluorescence spectra and detected the sample's structural changes via diffraction, observing the inverse volume collapse across the spin transition. During x-ray heating, the carbonate transforms into orthorhombic $Fe_4C_3O_{12}$ and iron oxides. Incipient melting was also observed. This approach to collect information about the electronic state and structural changes from samples contained in a diamond anvil cell at melting temperatures and above will considerably improve our understanding of the structure and dynamics of planetary and exoplanetary interiors.

DOI: 10.1103/PhysRevResearch.4.033042

I. INTRODUCTION

Probing the spin state of iron in oxides, silicates, or carbonates directly at pressures (P) and temperatures (T) expected at the Earth's lower mantle and core is of immense importance for our understanding of related physical and chemical properties such as density, elasticity, or element partitioning in relevant minerals at these extreme conditions [1]. Even though reaching melting temperatures of different materials in diamond anvil cells (DACs) is achieved routinely in combination with x-ray diffraction (XRD) using continuous or pulsed laser heating systems [2–5], the combination with measurements that are sensitive to the spin state and electronic structure in general, such as x-ray emission spectroscopy (XES), still poses a challenge. The measurement of the spin state of geologically relevant materials at high pressures becomes more difficult with increasing temperatures due to the necessity to keep the temperature stable over a long period of time. At third-generation synchrotron facilities, the usual exposure time to measure the spin state of Fe contained in a DAC via the Kβ fluorescence is of the order of minutes to tens of minutes, depending on the sample's iron content and photon flux [6]. Successfully keeping a sample at a constant temperature near its melting point with a spatially highly stable heating spot using regular laser heating methods while measuring the sample's electronic spin state has only been reported by a few research groups [7–10]. We performed a proof-of-principle experiment demonstrating an alternative approach for high P/T spectroscopy measurements of solids and melts, using the unique possibilities provided by a superconducting x-ray free electron laser (XFEL).

The brilliance of an XFEL, supplying highly intense photon pulses with a duration on the femtosecond timescale on a very small focus at a micrometer scale, opens up the possibility to heat samples using x rays. Through the rapid energy deposition from x rays on a sub-picosecond timescale, i.e., faster than thermodynamic expansion, it is possible to heat electrons of solid samples while the ion density stays constant.

*johannes.kaa@tu-dortmund.de

At longer timescales, heating of the lattice ions from electrons reaches a local thermodynamic equilibrium condition, which has only recently been exploited as a tool to heat samples contained in a tamper, such as a DAC [11–13]. Here, we describe the novel combination of x-ray heating of samples and the static pressurized environment of a DAC, to make simultaneous measurements of spin sensitive XES and structure sensitive XRD for the case of $FeCO_3$.

The stability of $FeCO_3$ at lower mantle P/T conditions and beyond has been experimentally explored thoroughly [14–20]. At ambient P/T conditions, $FeCO_3$ forms the common trigonal mineral siderite consisting of Fe^{2+} cations and planar trigonal CO_3^{2-} anions and its structure remains stable up to approximately 120 GPa. From 43 to 47 GPa, the spin state of the Fe cation changes from high spin (HS) to low spin (LS) (see Ref. [21] and references therein), which is connected to a volume collapse of the unit cell by about 10 % [22]. When heated from 1800 to 2100 K at pressures between 25 to 43 GPa, the HS-$FeCO_3$ will in most cases incongruently melt under the formation of the high pressure form of Fe_3O_4 [23] and diamond. Above the pressure-induced spin change, and up to 70 GPa, a temperature-induced reversal of the spin-associated volume collapse takes place at temperatures above 500 K [18]. The formation of orthorhombic $Fe_4C_3O_{12}$, a phase with tetrahedral CO_4^{4-} anions, was found during experiments above 50 GPa and 1300 K [16] and was predicted by simulations [20]. Above 70 GPa, $Fe_4C_4O_{13}$, another high-temperature phase including tetrahedrally coordinated carbon, becomes stable [18,24,25]. Previous work on $Fe_4C_3O_{12}$ and $Fe_4C_4O_{13}$ at lower mantle pressures shows iron in a HS state both at high temperatures and after quenching [6], in agreement with DFT simulations [6,20]. The appearance of tetracarbonates in the $FeCO_3$ system has always been reported together with Fe oxides, however, the role of Fe_xO_y in varying stoichiometry, and especially the spin state, at lower mantle conditions is still disputed and has been reinvestigated by multiple research groups [26–29].

The presented experiment provides a scheme to access unique information about the electronic state and local structure in the Fe−C−O system at extreme P/T conditions from the solid to the melt. It also sets a benchmark for future microsecond time-resolved emission spectroscopy measurements using a DAC coupled with a pulsed x-ray beam from a superconducting XFEL facility at the High Energy Density (HED) instrument at EuXFEL. This ultimately enables pump-probe x-ray emission experiments at timescales and P/T conditions beyond what can be reached with well-established approaches.

II. EXPERIMENTAL SETUP

A. Sample environment

A DAC of type Bx90 with a radial opening, specialized for fluorescence measurements through a side window perpendicular to the beam, was loaded with pure synthetic siderite powder [18] pressed into a pellet with a diameter of about 50 μm. The use of asymmetric seats [30] and a standard diamond in the upstream direction ensured an opening angle of approximately 25° for emission detection through a side window. Downstream, a Boehler-Almax diamond provided a large opening angle of 70° on the back of the DAC for XRD measurements (Fig. 1). The sample was contained inside a rhenium gasket and squeezed between two diamonds with a culet diameter of 300 μm. To optimize the sample environment geometry for the XES signal, the gasket preparation and sample loading was done as described in reports on earlier emission experiments [6,9,30,31]. Neon was loaded as a pressure-transmitting medium to ensure quasihydrostatic pressure conditions throughout the sample chamber. For the determination of the pressure, we used the fluorescence shift of a ruby single crystal that was placed next to the sample inside the gasket [32]. The measurements were performed at 51 ± 1 GPa, which was further confirmed after the experiment by measuring the optical Raman spectra of the diamond culet [33].

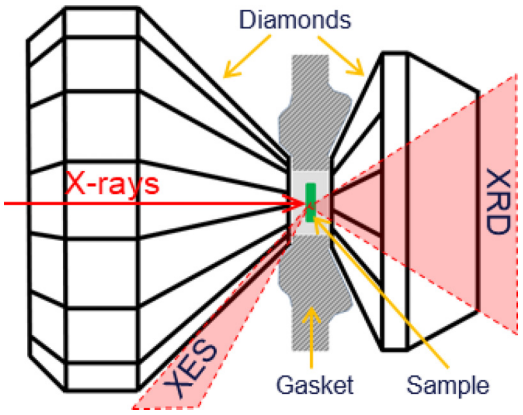

FIG. 1. DAC schematic with a 2.275-mm-wide standard diamond upstream and a 1.72-mm-wide Boehler-Almax diamond downstream. The sample (green) is contained in a hole in the Re gasket with a diameter of 100 μm. The recorded XES signal passes out of the DAC through the standard diamond and a side window in the DAC housing (not shown). The XRD signal was measured through the downstream Boehler-Almax diamond.

B. X-ray heating in a DAC

The experiment was conducted at the HED instrument of the European XFEL [34,35]. The incident beam had a photon energy of $E = 13$ keV with a Self-amplified spontaneous emission (SASE) bandwidth of $\Delta E/E = 1 \times 10^{-3}$ and was delivered in 10 Hz trains, which contained up to ten pulses each at a maximum repetition rate of 2.2 MHz. The pulse energy of the femtosecond pulses was controlled by attenuating the beamline transmission to a maximum of 255.2 ± 4.5 μJ as determined by x-ray gas monitors (XGMs) [36], which corresponds to a photon flux of the order of 10^{11} ph/pulse. However, this value does not take the absorption of optical elements after the XGMs and of the upstream diamond of the DAC into account. The latter is estimated to absorb roughly 55% of the transmitted x-ray beam for a 2.2-mm-thick diamond at 13 keV [37]. A spot size of 20x20 μm (VxH, FWHM) at the target chamber center (TCC) of the interaction chamber 1 (IC1) was achieved using Be compound-refractive lenses located roughly 9 m upstream from TCC. An inline microscope and a hexapod positioning

system was used to align the DAC in the XFEL beam. The pressure inside IC1 was approximately 1×10^{-6} mbar during the experiment. The efficiency of heating with x-ray pulses within a train was controlled by altering the repetition rate of the incoming pulses [11]. To probe the sample at close-to ambient temperature conditions, we used a repetition rate of 455 kHz resulting in a time gap of 2.2 μs between the arrival of each pulse, i.e., sufficient time for the sample to cool down between x-ray pulses. The heating runs were conducted at 2.2 MHz, i.e., with 444 ns pulse spacing, which does not leave enough time for complete cooling of the sample in between pulses. It should be noted that pulse-to-pulse pointing instabilities and the Gaussian profile of the x-ray beam may cause probing of parts of the unheated sample. All runs mentioned in this paper are listed in Supplemental Material (SM) Table I [38].

III. METHODS

A. *In situ* measurement

The Fe $K\beta_{1,3}$ emission line at about 7 keV was measured with an energy-dispersive von Hámos spectrometer near 90° scattering geometry with emitted x rays passing through the standard diamond and the large open side window of the DAC housing. This geometry minimizes the elastically scattered radiation from the sample and the DAC on the detector, which decreases the scattering background, and creates an optimized field of view to detect the XES signal. It also reduces the absorption of the fluorescence by the diamond anvil, as the travel length through the diamond is minimized. The von Hámos spectrometer consists of a single cylindrically bent Si (531) analyzer crystal (110 × 30 mm (V×H) with a bending radius of 250 mm) that dispersed the fluorescence with a central Bragg angle of 72° onto an ePix100 detector with a pixel size of 50 × 50 μm and a repetition rate of 10 Hz [39,40], providing an energy window of roughly 150 eV. The energy calibration for the XES detector was conducted by fitting the $K\beta_{1,3}$ fluorescence line including the valence-to-core signal from a Fe foil to a reference Fe emission line [41]. The dispersion of the setup on the detector plane is 300 meV per pixel with a FWHM of 5 eV for the $K\beta$ main peak of the measured Fe foil.

XRD measurements were performed using a second ePix100 detector downstream of the DAC, providing a scattering angle (2θ) of 11.8° to 30° or a momentum transfer (Q) of 1.4 Å^{-1} to 3.4 Å^{-1}. To prevent saturation during exposure with several trains, the detector sensor was covered with a Cu foil of 20 μm thickness. The angular range of the detector was calibrated using a CeO_2 standard and the data was analyzed using DIOPTAS [42]. Each run lasted for roughly 3000 trains during which the XES and XRD detectors collected at 10 Hz repetition rate.

B. *Ex situ* and recovered samples analysis

1. XRD imaging

Spatial XRD mapping was performed at beamline P02.2 at PETRA III to identify phases in the quenched sample still contained in the DAC at 51 GPa. The XRD map had a step size of 2 × 2 μm. The incident beam with a photon energy of 42.7 keV was focused to 2 × 2 μm (VxH, FWHM) using Kirkpatrick Baez mirrors [43]. The grid size was 31 × 31 steps. Each step had an exposure time of 30 seconds while scanning over an ±5° Ω rotation around the vertical axis perpendicular to the x-ray propagation. The signal was collected with a 2D Perkin Elmer detector, which was calibrated using a CeO_2 standard. The maps were analyzed with the X-ray Diffractive Imaging software [44].

2. Raman spectroscopy

To further support the phase identification, the sample contained in a DAC, and recovered single grains at ambient pressure, were measured using a LabRAM HR800 VIS Raman spectrometer at Geoforschungs Zentrum (GFZ) Potsdam, utilizing a 532 nm laser. Raman spectra were collected in a range from 300 cm^{-1} to 1250 cm^{-1}. A complete map of the sample with a step size of 4 μm and a smaller map of the heating spot with a step size of 2 μm were taken. For both maps, each point was measured for 1 min.

3. XES imaging

To characterize the spin state of the entire temperature-quenched sample in the DAC, it was mapped at the P01 beamline at PETRA III. The incident beam had an energy of 10.4 keV and a beam size of 8 × 8 μm (VxH, FWHM) [45]. Using an energy dispersive von Hámos type spectrometer with four Si (440) cylindrically bent analyzer crystals (bending radius of 500 mm) at a central Bragg angle of 61° and a Pilatus 100K detector [9], we measured the Fe $K\beta_{1,3}$ fluorescence for 5 minutes for each step of a 6 × 6 grid. The step size was 8 μm.

4. Scanning electron microscopy and transmission electron microscopy

Several grains were recovered from the sample after opening the DAC for *postmortem* analysis, at GFZ Potsdam. The recovered grains were arranged on a glass slide and put into a Quanta 3D field emission gun scanning electron microscope to identify relevant grains with melting structures on their surface. Afterward, the sample was carbon coated and then cut into transmission electron microscopy (TEM) foils with a Helios G4 UC DualBeam. The TEM lamellae were further analyzed in a FEI Tecnai F20X-Twin TEM by imaging and analyzing electron diffraction patterns.

C. Temperature simulation

Using finite-element analysis provided by the simulation program COMSOL MULTIPHYSICS [11], we calculated the sample's temperature response to the absorption of the x-ray pulses during a single x-ray pulse-train at 2.2 MHz and 455 kHz, assuming the x-ray beam hits the sample in its center. We suppose a pulse duration of 30 fs and a Gaussian-shaped beam with a radius of 30 μm FWHM. The pulse energy was set to 15 μJ for 2.2 MHz and 5 μJ for 455 kHz to reach realistic temperatures at the time of probing by the subsequent x-ray pulse. Thermodynamic properties of the compressed $FeCO_3$ and the diamond anvils assumed in the model are given in SM Table II.

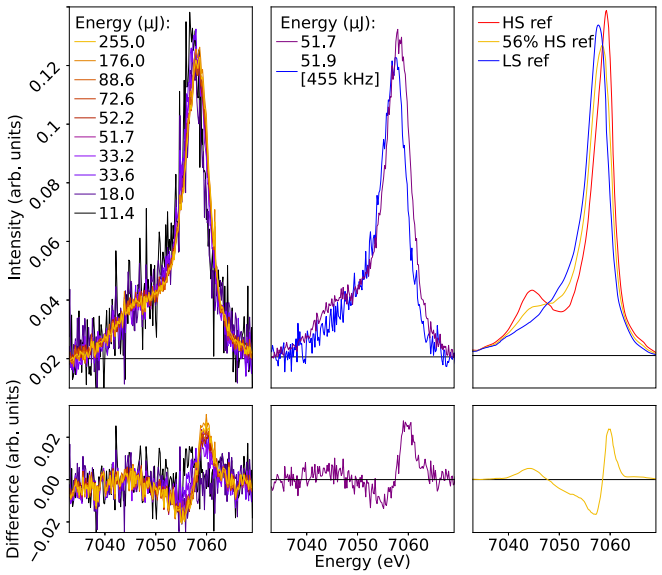

FIG. 2. Left: Raw emission signals for different runs (top) including the difference to a subtracted LS signal measured at 455 kHz (bottom). Center: Separated selected emission spectra for increased spin state compared to a low spin spectrum. Right: HS-reference and LS-reference of $FeCO_3$ [9] and a combination of 44% HS spectrum and 56% LS spectrum, resembling the run at highest used pulse energy. The difference between each spectrum and the LS spectrum is shown below.

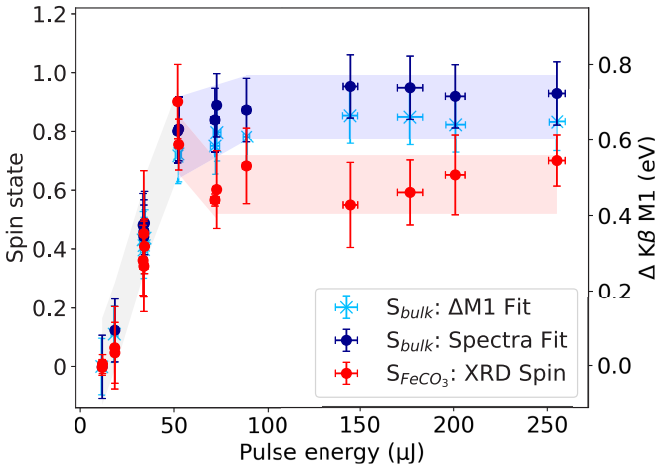

FIG. 3. The dependence of S_{bulk} as obtained by fitting of the ΔM1 shift (light blue), and by fitting of the raw XES spectra to the reference spectra (dark blue) to the pulse energy of the incident XFEL beam. The $FeCO_3$ diffraction peak intensity ratio (red) estimates the spin state of $FeCO_3$. The splitting of the blue and red shaded area above roughly 50 μJ is due to the decomposition of $FeCO_3$ and shows the effect of Fe bearing decomposition products on the spin state S_{bulk}.

IV. RESULTS AND DISCUSSION

A. *In situ* results at high P/T

Based on the configuration of the 3*d* electrons of the Fe cations, the absolute spin state change in our sample can be specified by the analysis of the $K\beta$ fluorescence line in terms of its energy shift and shape. The most prominent features are the $K\beta_{1,3}$ emission line and its satellite peak $K\beta'$, which depend on the exchange of the 3*d* valence electrons with the 3*p* electrons. Based on the spin of the 3*d* electrons of the Fe cation, the peaks act as an indicator of the total spin moment S_{bulk}. This change becomes visible in Fig. 2 (left) during the gradual increase of the pulse energy, i.e. increasing heating of the sample, and acts as an indicator for an increase of the fraction of HS Fe. By comparing the peak shape measured at ambient temperature and a heating run [Fig. 2 (center)] with the most prominent satellite peak to a LS and HS references [Fig. 2 (right)] [9], it becomes clear that a pure HS state has not been detected during the experiment. However, a combination of the LS and HS references provides a good fit of the peak shape. To be able to extract an accurate value of the spin state S_{bulk} from the raw spectra, the $K\beta_{1,3}$-first moment (M1) shift can be used [46], which is calculated by

$$M_1 = \frac{\sum_j (E_j I_j)}{\sum_j I_j},$$

with energy E_j and intensity I_j at point j for all points ±50 % of the maximum intensity of the $K\beta_{1,3}$ peak. It has been shown that the M1 value has a linear dependence on the commonly used integrals of the absolute values of the difference spectra (IAD) [46,47] and, therefore, on the spin change. In contrast to the determination of the spin state via IAD values, the M1 shift can be applied to spectral data of lower statistical quality. For the analysis, the spectra were aligned to the same center of mass. At 2.2 MHz, the spin state starts to change above an incident XFEL pulse energy of 18.1 μJ and reaches its maximum at 70 μJ, and it stays constant with increasing pulse energies. To estimate the absolute spin-state moment S_{bulk}, i.e., the average spin state of all iron-bearing compounds probed in the x-ray spot, we fitted each spectrum with a linear combination of $FeCO_3$ HS and LS reference spectra [9]. These reference spectra were measured at small pulse energies, which exclude the presence of thermally induced phase transitions or decomposition products. The resulting spin state was then linked to corresponding M1 shifts relative to the LS reference. Alternatively, the ΔM1 values can be linked to a S_{bulk} value via comparison to earlier measurements. The comparison of the respective spectra at increasing pulse energy to a HS reference spectrum shows that S_{bulk} reaches a maximum value of 0.9 ± 0.1 or 40 % to 50 % of the Fe^{2+} HS state of ambient temperature $FeCO_3$ (Fig. 3).

Diffraction patterns from runs taken at 455 kHz confirm that the sample consists solely of $FeCO_3$. At this repetition rate, the spin state change from the LS to HS state in $FeCO_3$ can only be observed at pulse energies above 51.8 ± 1.9 μJ to 78.4 ± 2.3 μJ, as manifested by the small peak at lower 2θ originating from the small fraction of the sample that underwent the inverse volume collapse (Fig. 4). Similar observations were reported by Lavina *et al.* [22], however, in that case caused by pressure gradients in their sample rather than by an increase in sample temperature. Even though the amount of HS-$FeCO_3$ is only a small fraction and the change in spin evaluated by the XES signal is negligible, the XRD data suggest that during ten pulses at 455 kHz, the heating was sufficient to induce a spin change. At a higher repetition rate

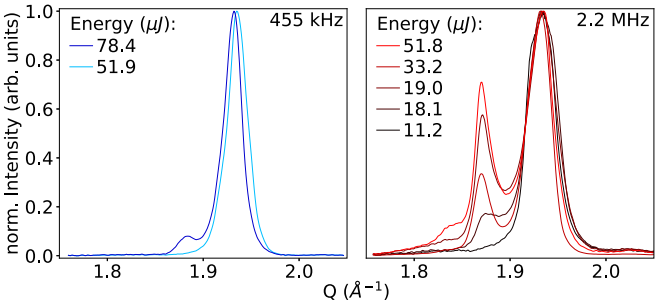

FIG. 4. Left: $FeCO_3$ (012) diffraction peak measured for 455 kHz runs. At 51.9 μJ, a single LS-$FeCO_3$ peak is visible. At 78.4 μJ, two peaks are observed which can be attributed to the LS-$FeCO_3$ and the HS-$FeCO_3$. Right: $FeCO_3$ (012) diffraction peaks measured for 2.2 MHz runs. In the XRD data at 11.2 μJ we see a single peak of the LS phase. Afterward, the peak splits into a LS/HS set with increasing HS portion. Example detector images for cold and hot runs are given in SM Fig. 1.

of 2.2 MHz, the appearance of the second set of diffraction peaks is already visible at 18.1 ± 1.8 μJ, due to less time for cooling in between pulses. The ratio of the intensity of HS- to LS-$FeCO_3$ diffraction peaks provides an estimate of the fraction of the spin state of the probed $FeCO_3$ and increases with rising sample temperature. This spin change is reversible by reducing the sample's temperature below 600 K, which causes the spin state of $FeCO_3$ to switch completely back to LS.

Figure 5 shows the simulations of the time-dependent temperature distribution during a ten-pulse train at 455 kHz and 2.2 MHz. Within the train, the temperature increases stepwise, with each x-ray pulse first probing the state of the sample cooled from the previous pulse and subsequently increasing its temperature due to absorption. During heating, the peak temperature can thus significantly extend the temperature of the sample during probing, so the experiments display not

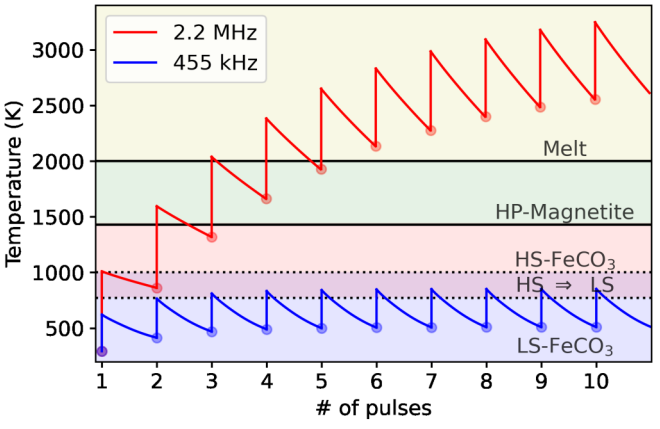

FIG. 5. Simulation of the heating cycle within each train at 2.2 MHz (red line) and 455 kHz (blue line). Circles mark the temperatures when the sample gets probed with XES and XRD. Phase stability fields at 51 GPa as suggested by Cerantola *et al.* [18] are indicated for LS-$FeCO_3$ (blue), HS-$FeCO_3$ (red), the spin state transition zone (violet), Fe_3O_4 (green), and melt (yellow).

only the sample's current state but also its heating history. The heating runs at 2.2 MHz show a steeper temperature increase at the moment of probing, potentially crossing the melting curve of $FeCO_3$ as suggested by Cerantola *et al.* [18]. The amount of HS-$FeCO_3$ was estimated by the intensity ratios of the diffraction peaks (Fig. 3) from the XRD data. When comparing the spin state S_{bulk} extracted from the XES spectra with the amount of HS-$FeCO_3$, the spin state determined by XES agrees well with the HS amount of $FeCO_3$ for pulse energies below 50 μJ. This is due to the lack of any other dominant phase in the system, which primarily consists of $FeCO_3$ up to roughly 50 μJ . When signs of melt and other phases become detectable in the XRD signal, the bulk spin state S_{bulk} and the HS-$FeCO_3$ content, determined by XRD, start to differ. S_{bulk} remains at a constant HS fraction of 45% while the HS fraction for the $FeCO_3$ signal decreases with increasing pulse energy. The discrepancy between HS-$FeCO_3$ and S_{bulk} may be attributed to the irreversible phase change from HS-$FeCO_3$ to other Fe-containing phases such as Fe oxides, $Fe_4C_3O_{12}$, or melt as further verified by *ex situ* XES measurements. At 33.6 ± 2.1 μJ, several other diffraction peaks appear that could be interpreted as Fe oxides like Fe_2O_3 in its double perovskite structure [48] and Fe_3O_4 (space group *Bbmm*) [23,29]. A definite assignment of these diffraction peaks is challenging due to the limited 2θ window and the overlapping peaks of these phases. An *in situ* diffraction pattern taken during heating can be seen in SM Fig. 2. At 51.8 ± 1.9 μJ, pulse energy diffraction peaks of $Fe_4C_3O_{12}$ start to appear and become more prominent with increasing pulse energy and heating. Above 88.7 ± 2.2 μJ, the high temperature phase CO_2−V (space group $I\bar{4}2d$) [49] can be observed. Signs of melt are evidenced by an intense and broad background signal underlying the diffraction peaks between 2.2 Å^{-1} and 3.0 Å^{-1} that appears in the XRD patterns at 51.8 ± 1.9 μJ and that becomes prominent relative to the crystalline phases with increasing pulse energy.

B. *Ex situ* and *postmortem* results

All phases that were identified *in situ* at high temperature were still present after quenching, except HS-$FeCO_3$ which undergoes a volume collapse to form LS-$FeCO_3$. XRD mapping was performed on the quenched sample with a 2 μm spatial resolution and allowed us to precisely determine the position of the heated spot, i.e., the area containing $Fe_4C_3O_{12}$ and CO_2−V. The location of the heating spot is evident from the low intensity of the diffraction peaks of the LS-$FeCO_3$ phase as this phase partially decomposed (Fig. 6). $Fe_4C_3O_{12}$ surrounds the center of the heated spot, whereas CO_2−V has crystallized in the center. Additional diffraction peaks may be assigned to Fe oxides, such as Fe_3O_4 or Fe_2O_3, however, definitive assignment is challenging because of the overlap of diffraction peaks of these phases. The presence of $FeCO_3$ and CO_2−V was further confirmed by optical Raman mapping in qualitative agreement with the XRD maps. Broad Raman bands from 250 cm^{-1} to 550 cm^{-1} and 690 cm^{-1} to 860 cm^{-1} were observed that are consistent with amorphous graphite and could result from graphitization of the diamond anvils. The same peaks were found during screening of the diamonds after pressure release and cleaning the anvil culets. We also

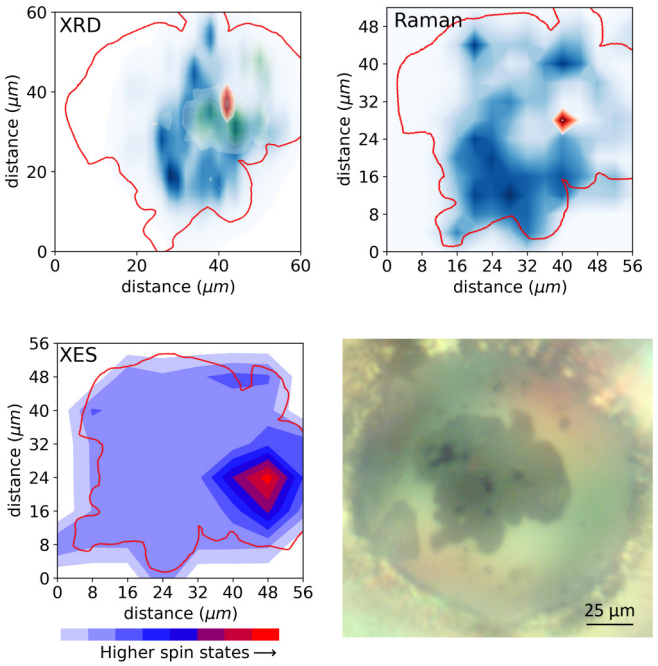

FIG. 6. Intensity-based phase distribution for the XRD (top left, see SM Fig. 3) and Raman (top right, see SM Fig. 5) maps. The main phase $FeCO_3$ (blue) has slightly lower intensities in the heating spot where $Fe_4C_3O_{12}$ (green) and $CO_2{-}V$ (red) appear. The XES map (bottom left, see SM Fig. 4) shows HS state in the heated spot relative to the surrounding LS-$FeCO_3$. The sample's approximate outline is marked in red. All measurements were conducted while still under high pressure. An image of the sample loaded in the DAC under a microscope is shown in the bottom right.

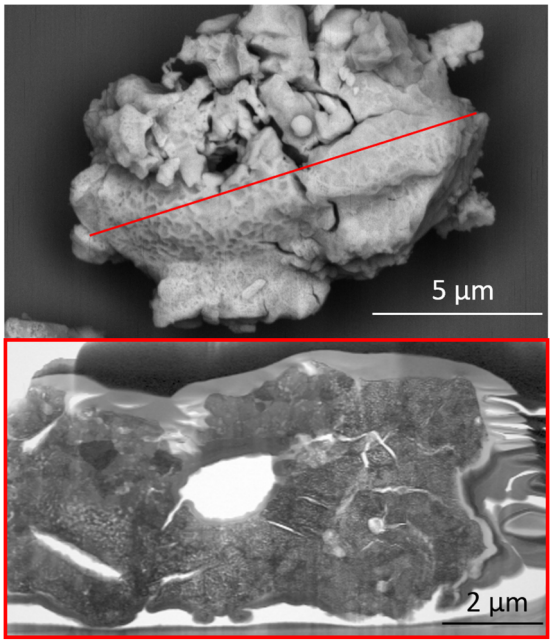

FIG. 7. Scanning electron microscopy picture of a recovered grain (top) with melting like structures on the grain's surface. The red line shows the position where the TEM foil was cut with a focused ion beam (FIB). The bright field image of the foil (bottom) shows Fe-oxide grains (grey) with very high porosity (white), suggesting degassing of CO_2.

noted an increase in the HS state in the quenched sample from the *ex situ* XES map with a measured maximum S_{bulk} of 1.3 ± 0.1 in the area where we found decomposition products. In the recovered sample outside the DAC, we identified Fe_3O_4 via optical Raman spectroscopy and Fe_2O_3 by electron diffraction on a TEM foil cut from a recovered grain. The surface of the grain shows a typical structure of solidified melt (Fig. 7, top). The TEM analysis showed a highly porous structure in bright field mode, suggesting degassing of CO_2 (Fig. 7). The position of the recovered grain relative to the heating spot could not be retraced.

It should be noted that while the upstream diamond showed localized graphitization from either radiation or thermal damages, the DAC retained its pressure during heating runs. After pressure release, the culet was found undamaged. This is a highly relevant technical aspect in terms of DAC experiments exploiting XFEL radiation.

C. Discussion on the reaction path

Our results imply very complex phase relations in the $FeCO_3$ system during multiple heating cycles up to melting temperatures followed by quenching. Since only pulse train averaged information from the *in-situ* XRD and XES measurements is available, a full understanding of all *in-situ* reactions is difficult. *Ex situ* and *postmortem* analyses have helped us to understand the processes retrospectively and have shone light on the highly complex nature of the $FeCO_3$ system at extreme conditions. Our results, both from *in situ* and *ex situ* analysis, suggest that, at pulse energies of $51.8 \pm 1.9\,\mu$J at 2.2 MHz, the following reactions occur during heating (T+) and quenching (T−):

$$\text{HS} - FeCO_3 \xrightarrow{\text{T+}} Fe_4C_3O_{12} \xrightarrow{\text{T−}} Fe_4C_3O_{12}.$$

Our data support a HS state of the hot and temperature quenched $Fe_4C_3O_{12}$ as reported by Albers *et al.* [6]. Above roughly $50\,\mu$J, with the appearance of amorphous signal on the XRD detector, our data suggest the reaction

$$Fe_4C_3O_{12} \xrightarrow{\text{T+}} \text{melt} + CO_2 \xrightarrow{\text{T−}} \text{Fe} - \text{oxides} + CO_2,$$

where the nature of the Fe oxides and the composition of the melt remains ambiguous. Although our data does not allow for a full and final understanding of the individual spin states of phases besides $FeCO_3$ due to the complexity and variety of different phases along the attained temperature path, it gives insight into the HS character of the combined decomposition products, including that of Fe in the melt.

V. CONCLUSION

In the present paper, we monitored the spin state and structure during decomposition of $FeCO_3$ at extreme pressures while generating high temperatures through x-ray heating at an XFEL facility. The sample reached melting temperatures during pumping and probing at 2.2 MHz at a fraction of the

available pulse energy. The simultaneously measured XRD expanded the information about the spin state of $FeCO_3$ by adding valuable data on the structural state and phase composition. At a repetition rate of 455 kHz $78.4 \pm 2.3\,\mu$J was sufficient to cause a temperature-induced spin change in $FeCO_3$ at roughly 600 K. At 2.2 MHz, the same heating-induced spin state change occurred at $18.1 \pm 1.8\,\mu$J, while at $51.8 \pm 1.9\,\mu$J our sample started to melt, suggesting temperatures above 3000 K [18]. The average spin state of Fe in all decomposition phases combined is above $S = 1$ and persists after quenching. Moreover, the data suggest the presence of Fe in HS in a Fe−C−O melt at 51 GPa. The energy threshold for nonthermal damage for diamonds [50] was not reached during the experiment. Thus the graphitization of the diamond anvils is likely caused by thermal damage which is currently under further investigation. Nevertheless, this experiment clearly shows the compatibility of using a DAC in combination with a highly focused and intense XFEL beam as a probe over tens of minutes. This successful proof-of-principle experiment allows us now to further improve our approach and the experimental setup for future measurements. It also marks a step toward microsecond time-resolved XES measurements from x-ray heated samples contained in a DAC and provides a probing scheme of the structure and spin state of melts at extreme static pressures by the combination of XES and XRD measurements. Such measurements permit the collection of highly relevant information for our understanding of the interior of planets in our solar system and beyond and will explore phase spaces on short timescales in future experiments at XFELs.

Data recorded for the experiment at the European XFEL are available at Ref. [51].

ACKNOWLEDGMENTS

We acknowledge European XFEL in Schenefeld, Germany, for provision of XFEL beamtime and would like to thank the staff for their assistance. We also acknowledge DESY (Hamburg, Germany), a member of the Helmholtz Association HGF, for the provision of experimental facilities. Parts of this research were carried out at PETRA III and we would like to thank Hans-Peter Liermann, Rachel Husband, and Konstantin Glazyrin for their assistance in using P02.2 ECB and Hlynur Gretarsson and Martin Sundermann for their support at the P01 beamline. We are grateful to the EuXFEL DAC Community and the HIBEF User consortium for the fruitful discussions. The use of equipment in the Potsdam Imaging and Spectral Analysis Facility (PISA) is gratefully acknowledged. The authors acknowledge financial support by the Federal Ministry of Education and Research of Germany (Project No. 05K19PE2). Parts of this project were financed by the Deutsche Forschungsgemeinschaft (Projects No. AP 262/1-2 and No. KO5262/1). Lelia Libon, Christian Albers, Robin Sakrowski, Christian Sternemann, and Max Wilke acknowledge the DFG for financial support via STE No. 1079/4-1 and STE No. 1079/2-1 as well as WI No. 2000/13-1, No. 2000/17-1, and WI No. 2000/8-2 within the DFG-FOR2125 CarboPaT. Christoph J. Sahle is thankful to the ESRF for support.

[1] *Deep Carbon*, edited by B. N. Orcutt, I. Daniel, and R. Dasgupta (Cambridge University Press, Cambridge, 2019)

[2] C. Sanloup, J. W. E. Drewitt, Z. Konôpková, P. Dalladay-Simpson, D. M. Morton, N. Rai, W. van Westrenen, and W. Morgenroth, Structural change in molten basalt at deep mantle conditions, Nature (London) **503**, 104 (2013).

[3] S. Petitgirard, A. Salamat, P. Beck, G. Weck, and P. Bouvier, Strategies for in situ laser heating in the diamond anvil cell at an X-ray diffraction beamline, J. Synchrotron Radiat. **21**, 89 (2013).

[4] A. Salamat, R. A. Fischer, R. Briggs, M. I. McMahon, and S. Petitgirard, *In situ* synchrotron X-ray diffraction in the laser-heated diamond anvil cell: Melting phenomena and synthesis of new materials, Coordination Chemistry Reviews **277-278**, 15 (2014).

[5] Z. Konôpková, W. Morgenroth, R. Husband, N. Giordano, A. Pakhomova, O. Gutowski, M. Wendt, K. Glazyrin, A. Ehnes, J. T. Delitz, A. F. Goncharov, V. B. Prakapenka, and H.-P. Liermann, Laser heating system at the extreme conditions beamline, P02.2, PETRA III, J. Synchrotron Radiat. **28**, 1747 (2021).

[6] C. Albers, R. Sakrowski, L. Libon, G. Spiekermann, B. Winkler, C. Schmidt, L. Bayarjargal, V. Cerantola, S. Chariton, N. Giordano, H. Gretarsson, J. Kaa, H.-P. Liermann, M. Sundermann, N. Thiering, M. Tolan, M. Wilke, and C. Sternemann, Fe^{3+}-hosting carbon phases in the deep Earth, Phys. Rev. B **105**, 085155 (2022).

[7] J.-F. Lin, G. Vanko, S. D. Jacobsen, V. Iota, V. V. Struzhkin, V. B. Prakapenka, A. Kuznetsov, and C.-S. Yoo, Spin transition zone in Earth's lower mantle, Science **317**, 1740 (2007).

[8] I. Kupenko, L. Dubrovinsky, N. Dubrovinskaia, C. McCammon, K. Glazyrin, E. Bykova, T. B. Ballaran, R. Sinmyo, A. I. Chumakov, V. Potapkin, A. Kantor, R. Rüffer, M. Hanfland, W. Crichton, and M. Merlini, Portable double-sided laser-heating system for Mössbauer spectroscopy and X-ray diffraction experiments at synchrotron facilities with diamond anvil cells, Rev. Sci. Instrum. **83**, 124501 (2012).

[9] C. Weis, G. Spiekermann, C. Sternemann, M. Harder, G. Vankó, V. Cerantola, C. J. Sahle, Y. Forov, R. Sakrowski, I. Kupenko, S. Petitgirard, H. Yavaş, C. Bressler, W. Gawelda, M. Tolan, and M. Wilke, Combining X-ray $K\beta_{1,3}$, valence-to-core, and X-ray raman spectroscopy for studying Earth materials at high pressure and temperature: The case of siderite, J. Anal. At. Spectrom. **34**, 384 (2019).

[10] G. Spiekermann, I. Kupenko, S. Petitgirard, M. Harder, A. Nyrow, C. Weis, C. Albers, N. Biedermann, L. Libon, C. J. Sahle, V. Cerantola, K. Glazyrin, Z. Konôpková, R. Sinmyo, W. Morgenroth, I. Sergueev, H. Yavaş, L. Dubrovinsky, M. Tolan, C. Sternemann *et al.*, A portable on-axis laser-heating system for near-90° X-ray spectroscopy: Application to ferropericlase and iron silicide, J. Synchrotron Radiat. **27**, 414 (2020).

[11] J. Meza-Galvez, N. Gomez-Perez, A. S. Marshall, A. L. Coleman, K. Appel, H. P. Liermann, M. I. McMahon, Z.

Konôpková, and R. S. McWilliams, Thermomechanical response of thickly tamped targets and diamond anvil cells under pulsed hard X-ray irradiation, J. Appl. Phys. **127**, 195902 (2020).

[12] H. P. Liermann, Z. Konôpková, K. Appel, C. Prescher, A. Schropp, V. Cerantola, R. J. Husband, J. D. McHardy, M. I. McMahon, R. S. McWilliams, C. M. Pépin, J. Mainberger, M. Roeper, A. Berghäuser, H. Damker, P. Talkovski, M. Foese, N. Kujala, O. B. Ball, M. A. Baron *et al.*, Novel experimental setup for megahertz X-ray diffraction in a diamond anvil cell at the high energy density (HED) instrument of the European X-ray free-electron laser (EuXFEL), J. Synchrotron Radiat. **28**, 688 (2021).

[13] H. Hwang III, T. Kim, H. Cynn, T. Vogt, R. J. Husband, K. Appel, C. Baehtz, O. B. Ball, M. A. Baron, R. Briggs, M. Bykov, E. Bykova, V. Cerantola, J. Chantel, A. L. Coleman, D. Dattlebaum, L. E. Dresselhaus-Marais, J. H. Eggert, L. Ehm, W. J. Evans *et al.*, X-ray free electron laser-induced synthesis of ϵ-iron nitride at high pressures, J. Phys. Chem. Lett. **12**, 3246 (2021).

[14] E. Boulard, A. Gloter, A. Corgne, D. Antonangeli, A.-L. Auzende, J.-P. Perrillat, F. Guyot, and G. Fiquet, New host for carbon in the deep Earth, Proc. Natl. Acad. Sci. USA **108**, 5184 (2011).

[15] V. Stagno, D. O. Ojwang, C. A. McCammon, and D. J. Frost, The oxidation state of the mantle and the extraction of carbon from Earth's interior, Nature (London) **493**, 84 (2013).

[16] J. Liu, J.-F. Lin, and V. B. Prakapenka, High-pressure orthorhombic ferromagnesite as a potential deep-mantle carbon carrier, Sci. Rep. **5**, 7640 (2015).

[17] V. Cerantola, C. McCammon, I. Kupenko, I. Kantor, C. Marini, M. Wilke, L. Ismailova, N. Solopova, A. Chumakov, S. Pascarelli, and L. Dubrovinsky, High-pressure spectroscopic study of siderite ($FeCO_3$) with a focus on spin crossover, Am. Mineral. **100**, 2670 (2015).

[18] V. Cerantola, E. Bykova, I. Kupenko, M. Merlini, L. Ismailova, C. McCammon, M. Bykov, A. I. Chumakov, S. Petitgirard, I. Kantor, V. Svitlyk, J. Jacobs, M. Hanfland, M. Mezouar, C. Prescher, R. Rüffer, V. B. Prakapenka, and L. Dubrovinsky, Stability of iron-bearing carbonates in the deep Earth's interior, Nat. Commun. **8**, 15960 (2017).

[19] V. Cerantola, M. Wilke, I. Kantor, L. Ismailova, I. Kupenko, C. McCammon, S. Pascarelli, and L. S. Dubrovinsky, Experimental investigation of $FeCO_3$ (siderite) stability in Earth's lower mantle using XANES spectroscopy, Am. Mineral. **104**, 1083 (2019).

[20] Z. Liand S. Stackhouse, Iron-rich carbonates stabilized by magnetic entropy at lower mantle conditions, Earth Planet. Sci. Lett. **531**, 115959 (2020).

[21] C. Weis, C. Sternemann, V. Cerantola, C. J. Sahle, G. Spiekermann, M. Harder, Y. Forov, A. Kononov, R. Sakrowski, H. Yavas, M. Tolan, and M. Wilke, Pressure driven spin transition in siderite and magnesiosiderite single crystals, Sci Rep. **7**, 16526 (2017).

[22] B. Lavina, P. Dera, R. T. Downs, V. Prakapenka, M. Rivers, S. Sutton, and M. Nicol, Siderite at lower mantle conditions and the effects of the pressure-induced spin-pairing transition, Geophys. Res. Lett. **36**, L23306 (2009).

[23] L. S. Dubrovinsky, N. A. Dubrovinskaia, C. McCammon, G. K. Rozenberg, R. Ahuja, J. M. Osorio-Guillen, V. Dmitriev, H.-P. Weber, T. L. Bihan, and B. Johansson, The structure of the metallic high-pressure Fe_3O_4 polymorph: Experimental and theoretical study, J. Phys.: Condens. Matter **15**, 7697 (2003).

[24] M. Merlini, M. Hanfland, A. Salamat, S. Petitgirard, and H. Müller, The crystal structures of $Mg_2Fe_2C_4O_{13}$, with tetrahedrally coordinated carbon, and $Fe_{13}O_{19}$, synthesized at deep mantle conditions, Am. Mineral. **100**, 2001 (2015).

[25] H. Piet, J. Badro, F. Nabiei, T. Dennenwaldt, S.-H. Shim, M. Cantoni, C. Hébert, and P. Gillet, Spin and valence dependence of iron partitioning in Earth's deep mantle, Proc. Natl. Acad. Sci. USA **113**, 11127 (2016).

[26] E. Bykova, L. Dubrovinsky, N. Dubrovinskaia, M. Bykov, C. McCammon, S. V. Ovsyannikov, H. P. Liermann, I. Kupenko, A. I. Chumakov, R. Rüffer, M. Hanfland, and V. Prakapenka, Structural complexity of simple Fe_2O_3 at high pressures and temperatures, Nat. Commun. **7**, 10661 (2016).

[27] R. Sinmyo, E. Bykova, S. V. Ovsyannikov, C. McCammon, I. Kupenko, L. Ismailova, and L. Dubrovinsky, Discovery of Fe_7O_9: A new iron oxide with a complex monoclinic structure, Sci. Rep. **6**, 32852 (2016).

[28] Q. Hu, D. Y. Kim, W. Yang, L. Yang, Y. Meng, L. Zhang, and H.-K. Mao, FeO_2 and FeOOH under deep lower-mantle conditions and Earth's oxygen–hydrogen cycles, Nature (London) **534**, 241 (2016).

[29] A. Bengtson, D. Morgan, and U. Becker, Spin state of iron in Fe_3O_4 magnetite and h$-Fe_3O_4$, Phys. Rev. B **87**, 155141 (2013).

[30] S. Petitgirard, I. Daniel, Y. Dabin, H. Cardon, R. Tucoulou, and J. Susini, A diamond anvil cell for X-ray fluorescence measurements of trace elements in fluids at high pressure and high temperature, Rev. Sci. Instrum. **80**, 033906 (2009).

[31] G. Spiekermann, M. Harder, K. Gilmore, P. Zalden, C. J. Sahle, S. Petitgirard, M. Wilke, N. Biedermann, C. Weis, W. Morgenroth, J. S. Tse, E. Kulik, N. Nishiyama, H. Yavaş, and C. Sternemann, Persistent octahedral Coordination in Amorphous GeO2 up to 100 GPa by Kβ'' X-Ray Emission Spectroscopy, Phys. Rev. X **9**, 011025 (2019).

[32] G. Shen, Y. Wang, A. Dewaele, C. Wu, D. E. Fratanduono, J. Eggert, S. Klotz, K. F. Dziubek, P. Loubeyre, O. V. Fat'yanov, P. D. Asimow, T. Mashimo, and R. M. M. W. and, Toward an international practical pressure scale: A proposal for an IPPS ruby gauge (IPPS-ruby2020), High Press. Res. **40**, 299 (2020).

[33] Y. Akahamaand H. Kawamura, Pressure calibration of diamond anvil raman gauge to 310 GPa, J. Appl. Phys. **100**, 043516 (2006).

[34] U. Zastrau, K. Appel, C. Baehtz, O. Baehr, L. Batchelor, A. Berghäuser, M. Banjafar, E. Brambrink, V. Cerantola, T. E. Cowan, H. Damker, S. Dietrich, S. D. D. Cafiso, J. Dreyer, H.-O. Engel, T. Feldmann, S. Findeisen, M. Foese, D. Fulla-Marsa, S. Göde *et al.*, The high energy density scientific instrument at the European XFEL, J. Synchrotron Radiat. **28**, 1393 (2021).

[35] W. Decking, S. Abeghyan, P. Abramian, A. Abramsky, A. Aguirre, C. Albrecht, P. Alou, M. Altarelli, P. Altmann, K. Amyan, V. Anashin, E. Apostolov, K. Appel, D. Auguste, V. Ayvazyan, S. Baark, F. Babies, N. Baboi, P. Bak, V. Balandin

et al., A MHz-repetition-rate hard X-ray free-electron laser driven by a superconducting linear accelerator, Nat. Photonics **14**, 391 (2020).

[36] T. Maltezopoulos, F. Dietrich, W. Freund, U. F. Jastrow, A. Koch, J. Laksman, J. Liu, M. Planas, A. A. Sorokin, K. Tiedtke, and J. Grünert, Operation of X-ray gas monitors at the European XFEL, J. Synchrotron Radiat. **26**, 1045 (2019).

[37] B. Henke, E. Gullikson, and J. Davis, X-ray interactions: Photoabsorption, scattering, transmission, and reflection at e = 50-30.000 eV, z = 1-92, At. Data Nucl. Data Tables **54**, 181 (1993).

[38] See Supplemental Material at http://link.aps.org/supplemental/10.1103/PhysRevResearch.4.033042 for (brief description).

[39] G. Blaj, P. Caragiulo, G. Carini, S. Carron, A. Dragone, D. Freytag, G. Haller, P. Hart, J. Hasi, R. Herbst, S. Herrmann, C. Kenney, B. Markovic, K. Nishimura, S. Osier, J. Pines, B. Reese, J. Segal, A. Tomada, and M. Weaver, X-ray detectors at the linac coherent light source, J. Synchrotron Radiat. **22**, 577 (2015).

[40] I. Klačková, K. Ahmed, G. Blaj, M. Cascella, V. Cerantola, C. Chang, A. Dragone, S. Göde, S. Hauf, C. Kenney, J. Segal, M. Kuster, and A. Šagátová, Radiation hardness study of the ePix100 sensor and ASIC under direct illumination at the European XFEL, J. Instrum. **16** (09), P09009.

[41] G. Hölzer, M. Fritsch, M. Deutsch, J. Härtwig, and E. Förster, $K\alpha_{1,2}$ and $K\beta_{1,3}$ X-ray emission lines of the 3d transition metals, Phys. Rev. A **56**, 4554 (1997).

[42] C. Prescher and V. B. Prakapenka, DIOPTAS: A program for reduction of two-dimensional X-ray diffraction data and data exploration, High Press. Res. **35**, 223 (2015).

[43] H.-P. Liermann, Z. Konôpková, W. Morgenroth, K. Glazyrin, J. Bednarčik, E. E. McBride, S. Petitgirard, J. T. Delitz, M. Wendt, Y. Bican, A. Ehnes, I. Schwark, A. Rothkirch, M. Tischer, J. Heuer, H. Schulte-Schrepping, T. Kracht, and H. Franz, The extreme conditions beamline P02.2 and the extreme conditions science infrastructure at PETRA III, J. Synchrotron Radiat. **22**, 908 (2015).

[44] R. Hrubiak, J. S. Smith, and G. Shen, Multimode scanning X-ray diffraction microscopy for diamond anvil cell experiments, Rev. Sci. Instrum. **90**, 025109 (2019).

[45] H.-C. Wille, H. Franz, R. Röhlsberger, W. A. Caliebe, and F.-U. Dill, Nuclear resonant scattering at PETRA III: Brilliant opportunities for nano – and extreme condition science, J. Phys.: Conf. Ser. **217**, 012008 (2010).

[46] S. Lafuerza, A. Carlantuono, M. Retegan, and P. Glatzel, Chemical sensitivity of $K\beta$ and $K\alpha$ X-ray emission from a systematic investigation of iron compounds, Inorg. Chem. **59**, 12518 (2020).

[47] G. Vankó, T. Neisius, G. Molnár, F. Renz, S. Kárpáti, A. Shukla, and F. M. F. de Groot, Probing the 3d spin momentum with X-ray emission spectroscopy: The case of molecular-spin transitions, J. Phys. Chem. B **110**, 11647 (2006).

[48] E. Bykova, M. Bykov, V. Prakapenka, Z. Konôpková, H.-P. Liermann, N. Dubrovinskaia, and L. Dubrovinsky, Novel high pressure monoclinic Fe_2O_3 polymorph revealed by single-crystal synchrotron X-ray diffraction studies, High Press. Res. **33**, 534 (2013).

[49] X. Yong, H. Liu, M. Wu, Y. Yao, J. S. Tse, R. Dias, and C.-S. Yoo, Crystal structures and dynamical properties of dense CO_2, Proc. Natl. Acad. Sci. USA **113**, 11110 (2016).

[50] N. Medvedev, H. O. Jeschke, and B. Ziaja, Nonthermal graphitization of diamond induced by a femtosecond X-ray laser pulse, Phys. Rev. B **88**, 224304 (2013).

[51] doi:10.22003/XFEL.EU-DATA-002560-00.